Tracking Epithelial Cell Junctions in *C. elegans* Embryogenesis With Active Contours Guided by SIFT Flow

Sukryool Kang*, Chen-Yu Lee, Monira Gonçalves, Andrew D. Chisholm, and Pamela C. Cosman

Abstract—**Quantitative analysis of cell shape in live samples is an important goal in developmental biology. Automated or semi-automated segmentation and tracking of cell nuclei has been successfully implemented in several biological systems. Segmentation and tracking of cell surfaces has been more challenging. Here, we present a new approach to tracking cell junctions in the developing epidermis of *C. elegans* embryos. Epithelial junctions as visualized with DLG-1::GFP form lines at the subapical circumference of differentiated epidermal cells and delineate changes in epidermal cell shape and position. We develop and compare two approaches for junction segmentation. For the first method (projection approach), 3-D cell boundaries are projected into 2D for segmentation using active contours with a nonintersecting force, and subsequently tracked using scale-invariant feature transform (SIFT) flow. The resulting 2-D tracked boundaries are then back-projected into 3-D space. The second method (volumetric approach) uses a 3-D extended version of active contours guided by SIFT flow in 3-D space. In both methods, cell junctions are manually located at the first time point and tracked in a fully automated way for the remainder of the video. Using these methods, we have generated the first quantitative description of ventral epidermal cell movements and shape changes during epidermal enclosure.**

Index Terms—**Active contours, *C. elegans*, cell junction tracking, embryogenesis, scale-invariant feature transform (SIFT) flow.**

I. INTRODUCTION

TRACKING cells or subcellular structures in developing embryos is important to understand developmental processes. Computer aided tracking allows quantitative analysis of large numbers of cells or objects and is of increasing importance in quantitative and systems developmental biology.

*S. Kang is with the Department of Electrical and Computer Engineering, University of California at San Diego, La Jolla, CA 92093-0407 USA (e-mail: srkang@ucsd.edu).

C.-Y. Lee and P. C. Cosman are with the Department of Electrical and Computer Engineering, University of California at San Diego, La Jolla, CA 92093-0407 USA (e-mail: chl260@ucsd.edu; pcosman@ucsd.edu).

M. Gonçalves is with the Department of Electrical Engineering, Rio de Janeiro State University, Maracanã, Rio de Janeiro 21941590, Brazil (e-mail: moniragoncalves@gmail.com).

A. D. Chisholm is with the Division of Biological Sciences, Section of Cell and Developmental Biology, University of California at San Diego, La Jolla, CA, 92093-0368 USA (e-mail: chisholm@ucsd.edu).

Recently, several automated or semi-automated nuclei tracking algorithms [1]–[3] that allow quantitative analysis of nuclear positions in the nematode *Caenorhabditis elegans* have been developed. However, nuclear positions do not provide direct information on cell shape, size, or cellular contacts. Thus, a major remaining challenge is to segment and track cell surfaces or contacts in 3-D space over time.

Here, we focus on epidermal epithelial cells in embryos of *C. elegans*. Like all epithelial cells, *C. elegans* epidermal cells display apical–basal cell polarity, such that the apical surface faces outwards from the embryo and the basal surface contacts an internal basal lamina. Epithelial cells are tightly connected by adhesive cell–cell junctions, one component of which is the protein DLG-1. When visualized from the apical or basal orientation, each cell appears outlined by a ring of DLG-1 at the apical or subapical level [see Fig. 1]. In this paper, we refer to cell boundaries or perimeters as defined by the localization of subapical junctional markers such as DLG-1.

Over the past decade, numerous automated or semi-automated algorithms for cell boundary segmentation in two or three dimensions (2D or 3D) have been developed. Active contours [4], [5], watersheds [5], [6], gradient-curvature driven flow [7], and subjective surface techniques [8] have been used to segment membranes in 2-D images. For 3-D images, active surfaces [9], watersheds [10], [11], gradient-curvature driven flow [7], subjective surface techniques [12], and polygon model fitting combined with image thresholding [13] have been used to segment cell surfaces. Most of the algorithms require labeling of the entire cell surface to construct cellular shape. Watershed methods, gradient curvature driven flow, and subjective surface techniques require detection of seed points that are enclosed by continuous surfaces. A region from the seed point is expanded until the growing region meets neighbor regions from other seed points or the region reaches the limit of the object. In contrast, labeling of subapical junctions in the *C. elegans* embryo does not provide information on the entire cell surface or even all points of cell–cell contact, precluding use of many of the seed-point-based methods.

An additional challenge in the *C. elegans* data is that the junctions of individual cells are not confined to a 2-D focal plane. In imaging data where the overall curvature of the sample is small with respect to the region of interest, projection of the 3-D data to a 2-D plane allows segmentation of cells in a 'quasi-2D' setting, as used in several studies of *Drosophila* epithelial junctions [14]–[18]. However, the high degree of curvature of the *C. elegans* embryo and cells makes a simple 2-D projection
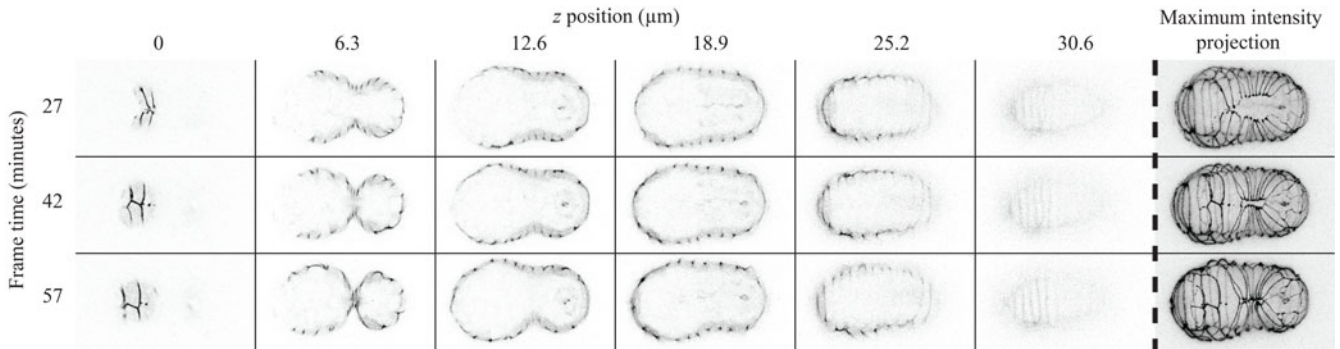
Fig. 1. Confocal *z*-stacks showing DLG-1::GFP embryos during epidermal enclosure. (The actual fluorescence data is imaged as bright pixels on dark background; for display purposes, we invert the gray scale to show dark signals on a white background.) Each row represents a single time point and each column shows a single *z*-slice. The final column shows the maximum intensity projection for each row.

challenging. We, therefore, needed to develop new methods to track cell boundaries in highly curved 3-D movies.

In this paper, we present two related methods to segment epithelial junctions in 3-D movies. Both methods are based on the fundamental concept of active contours or snakes [19]. A snake is a curve controlled by internal elasticity and image forces that pull the curve towards object contours. We generate initial contours for epithelial junctions manually at the first time point and then track the junctions with snakes guided by scale-invariant feature transform (SIFT) [20] flow in 2-D (projection approach) and 3-D (volumetric approach) space. A preliminary version of this study is in [21].

The contributions of this paper are in several areas. First, this paper presents the first algorithm that provides fully automated tracking (following initialization in the first frame) of epithelial junctions in highly curved 3-D datasets over time. Second, we develop algorithmic innovations in the use of a nonintersecting force (NIF) for snakes which improves tracking of narrow cells. We also demonstrate the use of SIFT flow in 2-D and 3-D cell tracking. A third contribution is in evaluation methods, since we apply mean absolute deviation to compare cell contours, and we provide a comparison of projection and volumetric approaches to cell tracking and feature extraction. In the biological domain, computational modeling of epithelial cell shape changes in other organisms such as *Drosophila* has led to numerous insights into mechanisms of tissue morphogenesis, and has relied heavily on automatic analysis of cell boundaries and shapes [17], [22], [23]. Our study provides a first step towards similar computational analysis of *C. elegans* embryonic epidermal enclosure, including precise measurements of displacement and changes in cell perimeter, surface area, and compactness.

II. DATA ACQUISITION

Fluorescently-labeled *C. elegans* embryos were recorded by time lapse 4-D microscopy with confocal laser scanning microscopes. The subapical junctions of epidermal cells on the embryo surface were marked with the transgene *xnIs17* [24], which expresses green fluorescent protein (GFP) fused to the DLG-1 protein. DLG-1::GFP is visible as an irregular 3-D lattice of lines approximately 1 μm in width. We used Zeiss LSM700 or

LSM710 confocal microscopes equipped with $100 \times$ NA 1.46 oil immersion objectives. We segmented and analyzed three embryos (datasets) in the paper. Datasets 1, 2, and 3 have 3-D stacks of $512 \times 275 \times 35$, $512 \times 275 \times 35$, and $512 \times 256 \times 35$ voxels with resolutions of 0.125 μm $\times$ 0.125 μm $\times$ 0.9 μm, 0.125 μm $\times$ 0.125 μm $\times$ 0.9 μm, and 0.15 μm $\times$ 0.15 μm $\times$ 0.85 μm, recorded at intervals of 180 s, 90 s, and 180 s, respectively.

III. METHODS

Our goal was to develop tools for quantitative analysis of epithelial cell shape changes in 3-D samples such as the *C. elegans* embryo, and we begin with the development of algorithms for tracking cell junctions over time. In this study, we image DLG-1::GFP-labeled junctions of epidermal cells on the ventral embryo surface [see Fig. 1]. The images of junctions in our 4-D movies are often low and variable intensity, resulting in incomplete contours. These incomplete contours can be completed using snakes [19]. A snake is a curve that moves towards object outlines controlled by internal forces such as elasticity and rigidity as well as by image forces such as edges of objects in the image. The missing signals can be completed by using internal forces that make the contour smooth. In the original active contour model [19] developed for 2-D datasets, the snake was represented by a set of n points $v_i = (x_i, y_i), i = 1, \ldots, n$. To detect epithelial junctions in the 3-D stack, we extended the snake to three dimensions represented by a set of n points $v_i = (x_i, y_i, z_i), i = 1, \ldots, n$. The contour deforms to minimize the energy functional

$$E^*_{\text{snake}} = \sum_{i=1}^{n} E_{\text{snake}}(v_i)$$

$$= \sum_{i=1}^{n} E_{\text{internal}}(v_i) + E_{\text{image}}(v_i) + E_{\text{con}}(v_i). \quad (1)$$

E_{internal} represents the internal energy of the contour due to the bending, E_{image} represents the image forces, and E_{con} denotes the external constraint forces. The internal energy of

the contour is written as

$$E_{\text{internal}}(v_i) = \frac{1}{2}(\alpha\|v_i - v_{i-1}\|^2 + \beta\|v_{i-1} - 2v_i + v_{i+1}\|^2)$$
(2)

where we define $v_0 = v_n$ and $v_{n+1} = v_1$. The first term will have a large value if there is a gap in the curve (i.e., two successive points are spaced far apart). The weighting factors α and β control the relative penalty of stretching and bending. A large value of α will increase the internal energy as the contour stretches. A small value of α will make the contour less sensitive to the amount of stretch. The second term makes the contour smooth by reducing contour oscillations. The second term will have a large value if the contour is bending sharply. E_{image} represents the image force and is defined as

$$E_{\text{image}} = w_{\text{line}}I(x, y, z) + w_{\text{edge}}|\nabla I(x, y, z)|^2$$
(3)

where w_{line} and w_{edge} are weighting factors. The first term is the image intensity itself, which pushes the snake to align with the brightest nearby pixels. The second term (edge attraction) uses image gradients and pushes the snake to be attracted to image edges. In the volumetric approach (described in detail below), to determine the weighting factors, we tested values of α and β equal to 0.005, 0.01, 0.02, 0.03, 0.04, 0.05, 0.1, and 0.2 in conjunction with the values of w_{line} equal to 0, 0.5, ..., 2.5, 3 and the values of w_{edge} equal to 3, 3.5, ..., 5.5, 6, and determined that $\alpha = 0.01$, $\beta = 0.01$, $w_{\text{line}} = 1$, and $w_{\text{edge}} = 5$ yielded optimal results as evaluated using methods discussed in Section IV. In the projection approach, we tested values of α and β equal to 0.005, 0.01, 0.05, 0.1, 0.15, 0.2, 0.25, and 0.3 and values of w_{line} equal to 0, 0.001, 0.05, 0.1, 0.2, 0.3, 0.4, and 0.5 and w_{edge} equal to 1, 1.5, 2, 2.5, 3, 3.5, and 4, and we chose α of 0.2, β of 0.2, w_{line} of 0.05, and w_{edge} of 2 as yielding the best result. E_{con} denotes the external constraint forces; E_{con} can be used to guide the contour towards or away from specific features. In our study, a NIF was used as an external constraint as described in Section III-C.

We compared two related approaches based on snakes to track epithelial junctions. The projection approach uses 2-D maximum intensity projection images [last column in Fig. 1] to segment cell boundaries. The resulting 2-D boundaries are back projected into 3-D space. The volumetric approach uses the original 3-D image z-stack instead of a 2-D maximum projection. The projection approach is computationally simple and requires less user effort to generate initial contours. Working on the 3-D stack requires more computation and more user effort to generate initial contours; however, the volumetric approach reduces errors introduced by the projection process.

The tracking process is presented in Fig. 2. All processes are fully described in Sections III and IV. Our contour tracking software, ContourTracker4D, is implemented in MATLAB (MathWorks, Natick, MA, USA) and is available as an open source project at Sourceforge (https://sourceforge.net/projects/contourtracker4d/).
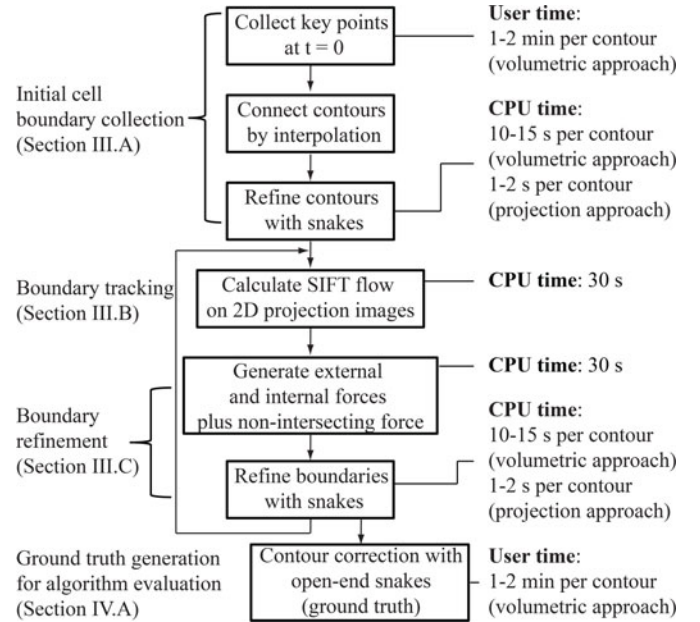

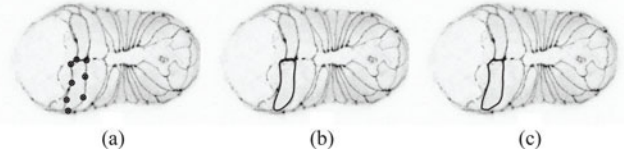Fig. 2. Flowchart and estimates of processing time for each step.

Fig. 3. Initial contour collection in a maximum intensity projection image. (a) Key points along the boundary are manually selected. (b) Selected points are connected into a closed contour using low pass interpolation. (c) Snakes are applied to refine the interpolated contour.

A. Initial Cell Boundary Collection

In either the projection or volumetric approaches, the initial positions of the cell boundaries must be defined by the user. Users manually define key points on the initial contour, as described below. Snakes are then applied to refine the contour defined by the key points. Both the projection and volumetric approaches do not need any further user input after this initial contour generation, and will track all cell boundaries automatically until the end of the video sequence. These steps will be described in more detail below.

1) Projection Approach: In the projection approach, we use 2-D maximum intensity projection images to track contours. After projecting the maximum pixel intensity of the top half of the stack (slices 1 to 17), some key points along the boundary of each cell are manually selected [see Fig. 3(a)] and are connected into a closed contour by low pass interpolation [see Fig. 3(b)]. In Fig. 3(a), eight points are manually selected. Seven–ten points are enough to generate the initial contour for most cells except for the large cell hyp7(18 + 19) [to the right of the example cell in Fig. 3(a)]. We use the interp function in MATLAB to perform low-pass interpolation for each dimension separately; the interpolated contours have ten times as many points as the selected key points. Finally, we refine these interpolated cell boundaries using snakes [see Fig. 3(c)]. This approach quickly

generates initial cell boundaries at the first time point with minimal curation.

2) Volumetric Approach: The original *z*-stack derived from LSM confocal data has lower *z* resolution than *xy* resolution. We therefore first render each *z*-stack isometric by applying linear interpolation along the *z* axis. The initial contours are identified manually with a visualization tool that displays each *z* slice, allowing the user to select sequential points on the contour. In the display, adjacent *z* slices are superimposed on the current *z* slice, which makes it possible to see both the small junction segments in the current slice as well as their continuations in the neighboring slices. For display purposes only, the tool connects the selected key points with a straight line and displays the connection in the 3-D stack whenever new points are added. Due to the higher number of degrees of freedom, about twice as many points are used to generate the initial contour as in the projection approach. After collecting key points for each cell, we apply low pass interpolation as in Section III.A.1 to obtain a contour based on points uniformly distributed at five pixel intervals. We then apply snakes to refine the interpolated points. Identical sampling processes are applied at the subsequent time instants during tracking to obtain uniformly distributed points.

B. Tracking

Given a cell boundary at a certain time, we aim to track its location to the next time. Optical flow [25] is a feature matching technique that computes motion patterns of two consecutive images under the assumption of small displacement. In such methods, optical flow is computed for the video data and then is used to estimate object movement. For example, given an object point (x, y) at time t with optical flow (u, v), one can estimate the same object point at time $t + 1$ will be at $(x + u, y + v)$. Although optical flow works reasonably well for most of the cell junctions tracked here, some cell boundaries move too much between successive time points for optical flow to work. To handle these large displacements, we need to use a more distinctive image feature representation instead of raw pixel values to provide more information. SIFT [20] is a popular image feature representation in computer vision and image processing. SIFT features [26] encode image gradient orientations around each point of interest, and therefore provide more general and robust structural information. SIFT flow replaces raw pixel values with SIFT features, and then performs a modified optical flow algorithm based on those SIFT features.

In the projection approach, we use 2-D SIFT to track *x* and *y* components in the 2-D projection image. In the volumetric approach, due to the large number of voxels in our datasets, computing 3-D SIFT and matching between two consecutive frames is too complex. So for the volumetric approach, we still begin with 2-D SIFT in the 2-D projection image to track *x* and *y* components. After tracking *x* and *y* components, the corresponding *z* values are taken to be the actual *z* values which are saved for every (x, y) point in the 2-D projection image when the 2-D maximum intensity projection was applied. Due to the errors introduced by projection, we compare *z* values at the previous frame with the tracked *z* value at the current frame.
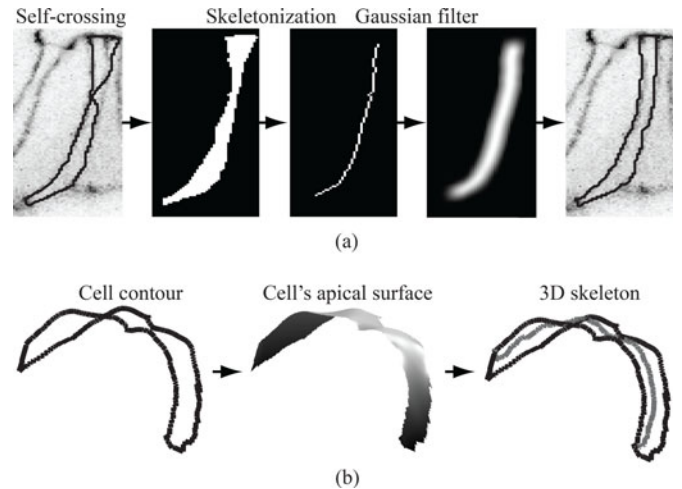

Fig. 4. NIF. (a) (Left) An example of self-crossing after applying snakes. (Middle images) Visualization of procedure that generates the NIF. (Right) Contour after applying snake with a NIF. (b) Visualization of procedure that generates the 3D skeleton.

If the difference between the two values is larger than a threshold (20 pixels), we use the *z* value at the previous frame instead of the tracked *z* value.

C. Boundary Refinement

Although SIFT flow provides improved tracking results over using optical flow, the tracked contour might still miss subtle details of contours. We apply snakes to align the tracked contours with true cell boundaries. Snakes also can produce incorrect segmentation results where contours are close together. We define self-crossing as occurring when the boundary of one side of a cell crosses or touches the boundary of the other side [left image in Fig. 4(a)]. We, therefore, added a NIF [see Fig. 4(a)] as an external constraint to avoid self-crossings in both the projection and volumetric approaches.

1) Projection Approach: We add a NIF to snakes as an external constraint to prevent self-crossing:

$$E_{\mathrm{con}} = w_{\mathrm{NIF}} \cdot E_{\mathrm{NIF}} \tag{4}$$

where w_{NIF} is a weighting factor. Fig. 4(a) shows the process to generate E_{NIF}. After filling the inside of the tracked contours, we apply a thinning operation to generate the skeleton. To avoid branches on the ends of the skeleton, we shrink the skeleton from all its end points until only two end points are left. Then, we grow out the two remaining end points along the unpruned skeleton by repeating a dilation operation to obtain the longest end-to-end path [27]. We then apply a Gaussian filter (size: 10×10 pixels, standard deviation: three pixels) on the skeleton image. E_{NIF} is normalized by the maximum value of the filtered skeleton image. Pixels close to the center line have stronger NIF than pixels far from the center line. To determine w_{NIF}, after selecting weight factors in (2) and (3), we tested values of w_{NIF} equal to $0.1, 0.2, \ldots, 0.9, 1$, and chose $w_{\mathrm{NIF}} = 0.3$.

When we apply snakes with a NIF, we solve the minimization of (1) using techniques of variational calculus described in [19]. The coefficients of the Euler–Lagrange equations are formed as
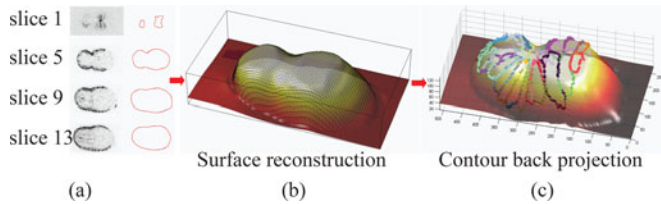
Fig. 5. 3-D embryo shape estimation and back projected contours: (a) Contours of the embryo surface for z slices. (b) Estimated surface. (c) Back projected contours on the surface.

Fig. 6. Contour correction via a manual correction tool.

a sparse matrix and the matrix is inverted to obtain the minimum energy of E^*_{snake} iteratively.

2) Volumetric Approach: To generate a NIF in 3-D space, we need to extend the skeleton image to 3-D space. When we have a contour in 3-D space [left image in Fig. 4(b)], we generate the 2-D skeleton on the 2-D projection image through the method in Section III-C1. The cell's apical surface is reconstructed as described in Section III-D [middle image in Fig. 4(b)]. For every (x', y') point on the 2-D skeleton, the (x', y', z') point on the cell's apical surface is considered to be part of the 3-D skeleton (a process we refer to as back projecting the 2-D skeleton) [right image in Fig. 4(b)]. We then apply a 3-D Gaussian filter (size: $7 \times 7 \times 7$ pixels, standard deviation: 1.5 pixels) on the 3-D skeleton. E_{NIF} is normalized by the maximum value of the smoothed image. To determine w_{NIF}, we tested values of w_{NIF} equal to $0.1, 0.2, \ldots, 0.9, 1$, and chose $w_{\text{NIF}} = 0.5$.

When we minimize (1), variational calculus in Section III-C1 is extended to 3-D space. Additionally, a greedy algorithm [28] option is available due to the complexity of variational calculus in 3-D space. Each point of each snake is moved within a small neighborhood ($3 \times 3 \times 3$) to the point which minimizes the energy function. In the neighborhood, all energy terms are normalized by the largest value separately. The energy function is computed for the current point and its new location will be the point that has the smallest value in its neighborhood. We repeat this operation until no more points are moved. This approach is computationally simple. If the initial contours are close to the epithelial junctions, this greedy algorithm produces results comparable to those from variational calculus. If the initial contours are far from the epithelial junctions, the greedy algorithm can cause more errors. We will compare the results from variational calculus and the greedy algorithm in Section IV.

D. 3-D Global Shape Reconstruction

To compute biological features in 3-D space, we reconstruct cells' apical surfaces on the embryo surface. The projection approach does the cell tracking in the 2-D projection image, but we then need to reconstruct the 3-D embryo surface at each time instant in the video. Since the original data only has scattered points on the embryo surface, we need to model the 3-D embryo surface at each time instant. We first extract contours of the embryo surface for each slice as shown in Fig. 5(a). The union of the set of contours can be considered as a point cloud of the 3-D embryo surface. We use the gridfit function [29] written in MATLAB to fit a smooth surface to the extracted point cloud. The
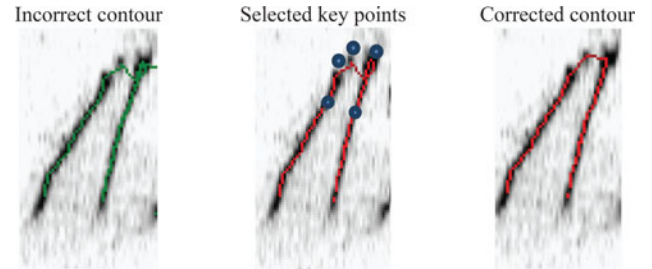
estimated surface is shown in Fig. 5(b). The estimated embryo shape allows us to estimate surface areas and cell perimeters.

After the surface reconstruction, the contour points in 2D are back projected on the reconstructed surface. We use the top half of the stack to reconstruct the top half of the embryo. The reconstructed surface has a one-to-one mapping for every pixel in the 2-D images [29]. After back projection, we can then have estimated 3-D locations of each contour as shown in Fig. 5(c). Cell surface areas and cell contour lengths can then be computed using these 3-D locations.

In the volumetric approach, unlike contour lengths, which can be computed directly from the 3-D contour points, cell apical surface areas require interpolation of the cell surface enclosed by the cell contour. We use the gridfit function on points of all cell contours without extracting the global contours of the embryo surface for each z slice.

IV. TRACKING EVALUATION

To evaluate and compare the tracking results of our algorithms, we need to generate ground truth. After generating ground truth, we analyze the tracking algorithm performance by calculating the mean absolute distance (MAD) [30] between the segmentation result and ground truth.

A. Generation of Ground Truth

We use a manual correction tool to generate ground truth at each time instant from the tracked cell contours [see Fig. 6]. After selecting the contour that we want to correct [left image in Fig. 6], we select multiple sequential points on the desired contour [middle image in Fig. 6]. The first point and the last point should be correct points of the segmented contour before the correction. When the first point and the last point are manually selected by clicking, the points might not be on the segmented contour, in which case the algorithm moves them to the closest point on the segmented contour. Then, an open ended snake is applied on the multiple sequential points to correct the contour [right image in Fig. 6].

At the first time instant, we generate 3-D ground truth through the initial cell boundary collection described in Section III-A2. Generating an initial cell boundary for a single cell takes approximately 2 min including the processing time for contour refinement via snakes. The generation of 24 initial contours takes approximately 40 min of user time; the snake processing time for 24 contours takes 4–5 min with a Six-Core Intel Xeon

2.8 GHz CPU. Compute time could be significantly reduced by using C instead of MATLAB. At the next time instant, the contours at the previous time instant are tracked via SIFT and refined via snakes with the volumetric approach. The average processing time of SIFT and snakes for 24 contours per frame is 5 min 15 s. After tracking and refining contours, we check 24 contours visually and correct wrong contours. On average, we corrected 9.5 out of 24 contours (39%) in each frame; however, it should be noted that only a small part of each contour required correction. The average time for the visual check and manual correction per frame is 13 min. The 3-D ground truth without the z component is considered to be 2-D ground truth and is used to check the tracking performance of the projection approach. When it comes to computation of biologically relevant features in Section V, we consider 3-D ground truth to be the most accurate ground truth, and compare the features from both the projection and volumetric approaches against those from 3-D ground truth.

B. Comparison of Tracking Methods

We analyze the tracking algorithm performance by calculating the MAD [30] between the segmentation result and ground truth. In [30], a metric to measure the distance $e(A, B)$ between two contours $A = \{a_1, a_2, \ldots, a_n\}$ and $B = \{b_1, b_2, \ldots, b_m\}$ is defined, where a_i and b_i are points sampled from curve A and curve B. The distance to the closest point on curve B for point a_i is defined as

$$d(a_i, B) = \min_j \|b_j - a_i\|. \qquad (5)$$

In [30], these distances are computed for all the points on the two curves and averaged to yield the MAD between two contours:

$$e(A, B) = \frac{1}{2} \left\{ \frac{1}{n} \sum_{i=1}^{n} d(a_i, B) + \frac{1}{m} \sum_{i=1}^{m} d(b_i, A) \right\}. \qquad (6)$$

We compute the MAD in units of pixels between the ground truth and the segmentation result for each frame.

We compare the tracking performances of the volumetric approach, the projection approach, and the 3-D back projection approach. A total of 24 contours on the ventral side are used to evaluate the algorithms. In Fig. 7, all tracking algorithms are initialized with ground truth at time 0 and are then allowed to proceed in fully automatic forward tracking mode with no manual correction. Figs. 7(a) and (b) show MAD with the volumetric approach. Comparing snakes with variational calculus, NIF, and SIFT flow, we find that MADs of most contours are less than three pixels distance except for six contours that have MAD from 3–6.5 [see Fig. 7(a)]. To compare algorithms, we use the averaged MADs for all contours at each time [see Fig. 7(b)]. It is evident that both optical flow and SIFT flow dramatically improve tracking accuracy. SIFT flow also shows better tracking accuracy than optical flow, although since SIFT's advantage is primarily for the few cells that move rapidly, the advantage appears small when averaged over all cells. To demonstrate SIFT's advantage, we measured MADs with SIFT and optical flow on hyp6(V), hyp6(VI), and hyp7(18–19) with the volumetric ap-

proach (variational calculus) [see Fig. 8]. These three cells move rapidly to enclose the head [see Fig. 9]. In an embryo recorded at 90-s interval, the MADs with SIFT flow remain less than 4 and most MADs with optical flow are in the range 4–6 [see Fig. 8(a)]. In embryos recorded at 180-s interval, rapidly moving cells have higher displacement and the MADs with optical flow reach 20 in the worst case while MADs with SIFT flow remain low (less than 5) [see Figs. 8(b) and (c)]. Use of variational calculus slightly improves segmentation over the greedy approach. The main advantage of the greedy algorithm is computational efficiency, as it is about ten times faster than variational calculus. The greedy algorithm takes about 30 s to track 24 contours per frame with a Six-Core Intel Xeon 2.8 GHz CPU. As the imaging interval for our movies is 90 to 180 s, the greedy algorithm can operate in real time, whereas variational calculus cannot. Use of the NIF helps avoid self-crossing; as such events are rare this improvement is not obvious at the level of the overall average MAD [see Fig. 7(b)].

Fig. 7(c) shows the MADs from the projection approach with variational calculus, SIFT flow, and NIF. To compute MADs, we use X and Y components of ground truth. Due to the fewer degrees of freedom, the MAD values (less than 1.4) remain lower than the results with the volumetric approach. Although the contours with the projection approach appear to show high accuracy, their 3-D back projected contours have high MAD values (larger than 18) [see Fig. 7(d)]. We plotted 3-D ground truth and 3-D back projected contours to visualize the errors. Fig. 7(e) (view from the top) shows 3-D back projected contours (blue) and 3-D ground truth (red) and the contours are almost identical. When the contours are rotated, the differences between 3-D ground truth and 3-D estimated contours are observed [see Fig. 7(f)]. In summary, both the projection and volumetric approaches are capable of accurate tracking (where accuracy is determined relative to 2-D and 3-D ground truth, respectively) when used with SIFT flow and a NIF. The 3-D back projected contours showed higher deviations from ground truth, largely because of errors in estimation of the surface. We, therefore, did not pursue 3-D back projection (of the projection approach) further, and in our analysis of biological features, compare only our projection and volumetric algorithms.

V. BIOLOGICAL FEATURE COMPUTATION AND RESULTS

To analyze the dynamics of epidermal ventral enclosure, we focused on epidermal cells that eventually make up the ventral side [see Fig. 9]. The ventral epidermis comprises a network of 24 cells each demarcated by lines of DLG-1::GFP that merge at cell–cell interfaces within the epithelium. We define the zero time in 4-D videos as the stage when the leading epidermal cells (hyp7 cells 18–19) have just fused into a single cell hyp7(18–19). About 30 min later, the entire embryo begins to rotate and elongate. When epidermal cells move left or right after the embryonic rotation, epithelial junctions may not be imaged clearly due to the lower resolution in the z direction. Because our projection approach is based on a 2-D projection of the top half of the image stack, it is not possible to segment cells on the left or right sides (i.e., the lateral seam epidermis). The volumetric
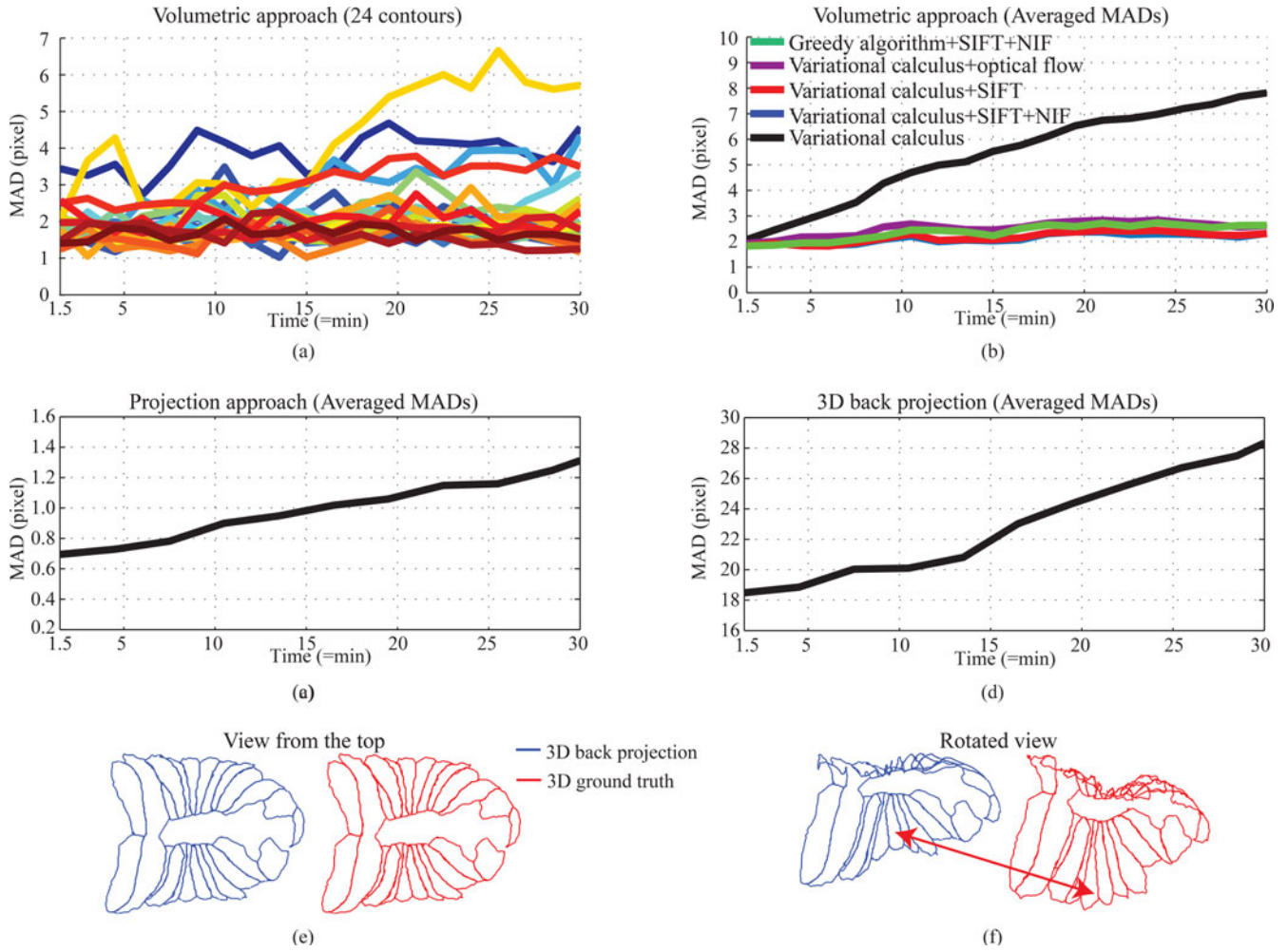
Fig. 7. Algorithm evaluation with mean absolute distance (MAD). (a) MADs for 24 contours with snakes (Variational calculus + SIFT flow + NIF). (b) Average value of MADs for all contours at each time instant with the volumetric approach. (c) Average value of MADs with the projection approach (Variational calculus + SIFT flow + NIF). (d) Average value of MADs with the 3D back projection. (e) Comparison of 3-D ground truth (red) and 3-D back projected contours (blue). (f) View from the side shows the difference in the mid-body.
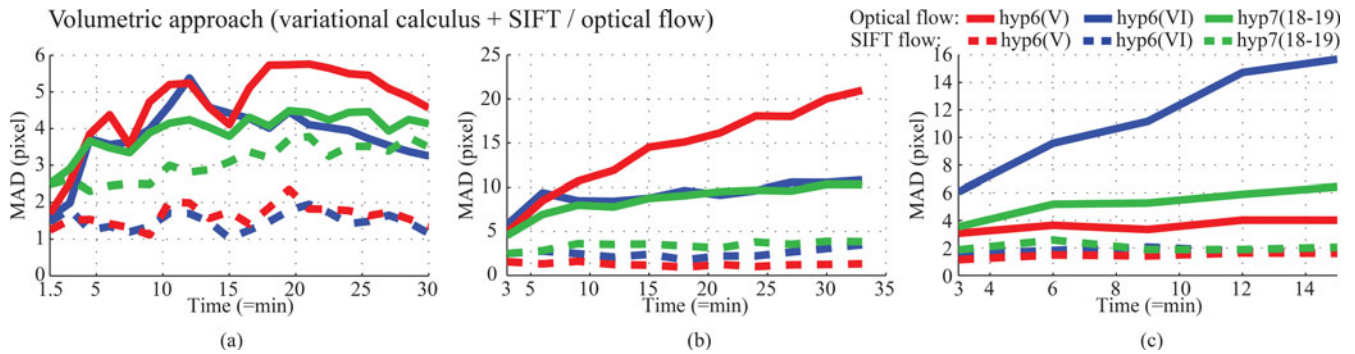

Fig. 8. Comparison of SIFT and optical flow on rapidly moving cells in three embryos. (a) MAD in embryo recorded at 90 s interval. (b), (c) MAD in embryos recorded at 180 s interval.

approach could allow tracking of lateral cells with sufficiently high pixel intensities, however due to the lower z resolution the junctional signals were not clear enough for efficient segmentation. We, therefore, restricted our analysis to the ventral epidermis. We compare features from 3-D ground truth and features from the projection and volumetric approaches, which are

fully automated after generating initial contours. An important goal was to determine how well the automated projection and volumetric tracking methods performed, with reference to our 3-D ground truth data. Below, we compare the performance of the two methods in terms of their depiction of quantitative trends in cell perimeter, apical surface area, and cell movement.
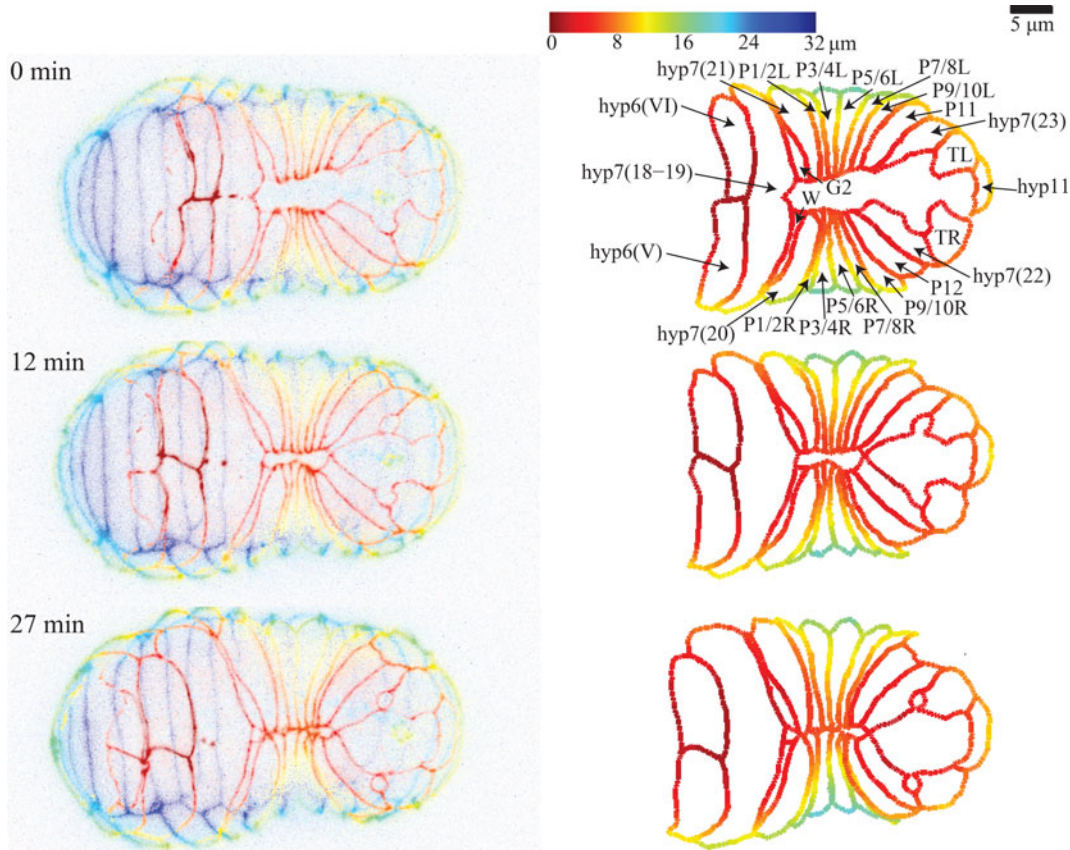
Fig. 9. Segmentation results for the 24 ventral epidermal cells, spanning the ventral half (15–16 μm) of the embryo in the *z*-axis. Contours are depth coded as indicated. (Left column) Maximum intensity projection image. (Right column) Results of ground truth of the 24 epidermal cells on the ventral side.

A. Cell Perimeter

The cell boundary length or perimeter as defined by DLG-1::GFP provides one indication of the change in cell size over time. We measured cell perimeters in three datasets (three embryos) using the ground truth, the volumetric approach, and the projection approach. Comparing the ground truth and the projection approach in the same embryo [left image in Fig. 10(a), showing left side cells only], it is apparent that the projection approach underestimates cell perimeter when contours are spread over many *z* slices (e.g., the P cells). The volumetric approach and the ground truth show similar cell perimeter except for hyp(18–19), G2, and hyp11 [see Fig. 10(a)]. These outlier cells have incorrect segmentation results due to their low pixel intensities or narrow cell width. Fig. 11 shows the segmentation errors of the narrow part of the G2 contour. The G2 contour increases by expanding the narrow part [first row in Fig. 11]. The projection and volumetric approaches do not produce correct segmentation results for the expanded contour because the snakes do not allow cell configurations in which the cells have long, narrow shapes unless they are initialized close to that configuration [second row in Fig. 11]. Nevertheless, using either approach, it is apparent that all ventral epidermal cells increase in perimeter during enclosure: ground truth shows overall a 9.4% increase (84 μm from 887.2 μm at $t = 0$) in total perimeter of 24 cells on the embryo in Fig. 9 and the volumetric and projection approaches show overall 2.8% (25.2 μm from 877.2 μm at

TABLE I
TOTAL PERIMETER OF 24 CELLS ON THE EMBRYO IN FIG. 9

Method	Cell perimeter (μm)		Increase (μm)
	at $t = 0$	at $t = 27$ min	
Ground truth	887.2	971.2	84.0 (9.4%)
Volumetric approach	887.2	912.4	25.2 (2.8%)
Projection approach	731.1	780.0	48.9 (6.7%)

$t = 0$) and 6.7% (48.9 μm from 731.1 μm at $t = 0$) increases, respectively, in Table I. For the average of all three embryos, ground truth, the volumetric approach, and the projection approach show overall 8.8% (78.4 μm from 891.3 μm at $t = 0$), 3.8% (33.7 μm from 891.3 μm at $t = 0$), and 8.2% (62.7 μm from 729.4 μm at $t = 0$) increases in cell perimeter, respectively.

To analyze the relative change in perimeter for individual cells, we normalized cell perimeters to the cell perimeter at $t = 0$. Most cells showed an increase in relative perimeter under either the volumetric or projection approaches, agreeing with ground truth [see Fig. 10(b)]. However, certain cells such as G2 show an increase in perimeter in ground truth but a decrease in the projection or volumetric approaches. This discrepancy arises due to errors in segmentation of the narrow part of the G2 contour [see Fig. 11]. Although the projection and volumetric approaches have segmentation errors on a small number of cells, when examined across all cells, both approaches have high correlation coefficients for cell perimeters (0.93–0.99) with ground
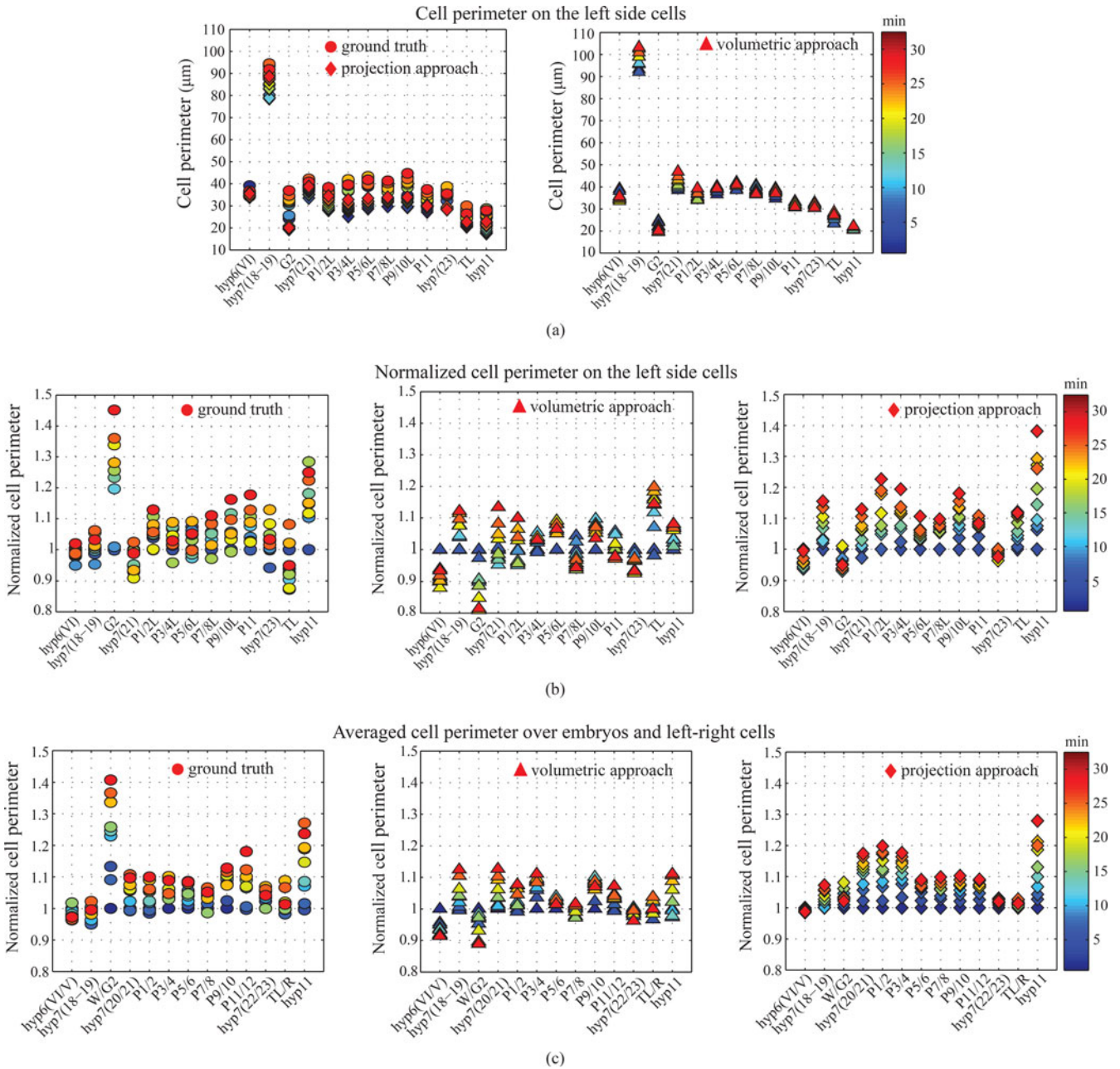
Fig. 10. Analysis of epidermal cell perimeter over time. Color bar represents the time from 0 to 30 min. Each *X* point with a cell name represents one individual cell. *Y* values show the change in cell perimeter over time. (a) Cell perimeters on the left side (Circles: ground truth, Diamonds: projection approach, Triangles: volumetric approach). (b) Normalized cell perimeters on the left side. Each cell perimeter was normalized by the perimeter at the start time. (c) Averaged cell perimeter over three embryos and left–right cells.

truth. To better visualize trends in the data, we plotted perimeters of four selected cells which are the leftmost cell (hyp6(V)), two middle cells (G2, P5/6L), and the rightmost cell (hyp11) [see Fig. 12]. Volumetric and projection approaches do not show an increase in cell perimeter for G2. The other three perimeters show similar trends between ground truth and volumetric and projection approaches.

We applied a Wilcoxon matched pairs test on the normalized cell perimeters to determine whether the three methods (ground truth, volumetric approach, and projection approach) are significantly different or not. We normalized 24 cell perimeters at the

last time point to the perimeters at $t = 0$. We used three embryos and applied a Wilcoxon matched pairs test on 72 ($=24 \times 3$) data points. *P* values between ground truth and volumetric approach and between ground truth and projection approach were less than 0.0001, and the *P* value between volumetric and projection approaches was 0.0483. The three different methods showed significant differences on the normalized cell perimeter. Both volumetric and projection approaches underestimated the normalized cell perimeters.

To compare the two approaches and derive an overall description of changes in cell perimeter, we averaged cell perimeter
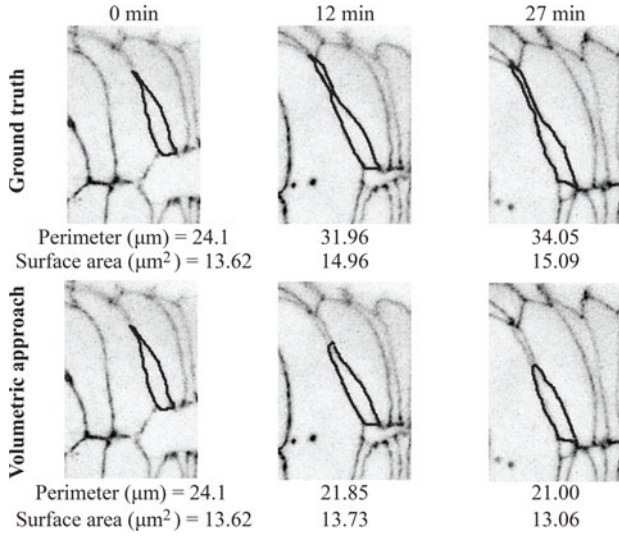
Fig. 11. Ground truth and segmentation result of G2. The volumetric approach has errors in segmentation of the G2 contour. The estimate of surface area is less sensitive to errors in segmentation of the narrow part.
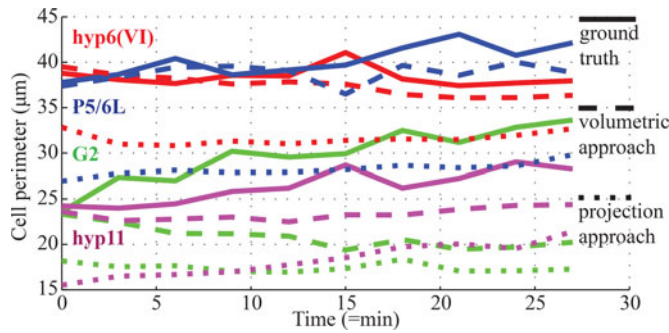

Fig. 12. Perimeters of four individual cells averaged over three embryos.

measurements over three embryos, keeping left and right cells separate. Correlation coefficients for the cell perimeter among three embryos were high (0.9–1). Correlation for 24 cell pairs (3-D ground truth) between embryos was calculated at each time. The correlation coefficients for left–right symmetric cell pairs range between 0.55 and 0.95. We averaged normalized cell perimeters instead of the cell perimeters [see Fig. 10(c)]. Overall, junctional contours increase by 10%–20% during ventral epidermal enclosure, consistent with the epidermal cells spreading, and increasing in apical surface area as they spread over substrate cells [left image in Fig. 10(c)]. The increase in cell perimeter for G2/W and hyp11 is higher than average [left image in Fig. 10(c)], likely reflecting the small size of these cells at the beginning of the video sequence. Comparing the two approaches and the ground truth, the projection approach [right image in Fig. 10(c)] yields better similarity to the ground truth [left image in Fig. 10(c)] than the volumetric approach [middle image in Fig. 10(c)]. The projection approach also yields slightly higher estimates for cell perimeter increases for P cells than the ground truth. Such discrepancies likely reflect the contribution of the z-axis to the cell perimeter (at $t = 0$).

B. Apical Surface Area

In the volumetric approach, we estimate apical surface area using cumulative patch areas based on the 3-D estimated surface and projected cell contour in 2-D space. We first extract the cell contour mask in the 2-D projection image. On the integer grid, there are square patches that have 1 pixel height and width. If all four points of each patch are inside the mask, we back project the patch on the reconstructed surface in Section III-D. We calculate each projected patch area by adding the areas of two triangles on the patch, and estimate apical surface area by summing all areas of the back projected patches. We calculated ground truth surface area with the identical method.

We computed apical surface areas from the three datasets and compared our two approaches and ground truth. The volumetric and projection approaches gave more consistent estimates of surface area [see Fig. 13(a)] compared to estimation of cell perimeter [see Fig. 10]. The greater consistency between the two methods is because our surface area measurement is less sensitive to errors in segmentation (e.g., G2) [see Fig. 11]. Errors in segmentation of the narrow part lead to large differences in the estimate of cell perimeter, but not large differences in the estimate of surface area. When we plotted the trends in surface area for four individual cells, we found that surface area shows more similar trends between ground truth and both methods [see Fig. 14] than cell perimeter [see Fig. 12]. Essentially, all ventral epidermal cells increase in surface area during enclosure: ground truth shows an overall 19.1% increase (204 μm^2 from 1065.4 μm^2 at $t = 0$) in epidermal surface area [embryo in Fig. 9] and the volumetric and projection approaches estimate 21.6% (230.2 μm^2 from 1065.4 μm^2 at $t = 0$) and 18.6% (119.5 μm^2 from 642.6 μm^2 at $t = 0$) increases respectively in Table II. For the average of all three embryos, the ground truth, the volumetric approach, and the projection approach show overall 19.1% (208.2 μm^2 from 1087.8 μm^2 at $t = 0$), 20.9% (227.5 μm^2 from 1087.8 μm^2 at $t = 0$), and 22.9% (151.3 μm^2 from 659.4 μm^2 at $t = 0$) increases in surface area. In contrast, the projection approach estimates a 10%–30% higher increase in surface area for P cells. This discrepancy results from the underestimation of initial surface area by the projection approach when cells are spread over multiple z slices.

We applied a Wilcoxon matched pairs test on the normalized surface areas of 72 data points (=24 contours $\times$ 3 embryos) to check the statistical significance of differences for three methods. P values between ground truth and volumetric approach, between ground truth and projection approach, and between volumetric and projection approaches were 0.1568, 0.1677, and 0.5625, respectively. P values showed that the differences were not statistically significant.

We next compared the consistency of the projection and volumetric approaches between different datasets. Cell surface areas display a correlation coefficient of 0.96–0.99 between embryos, whether the projection or volumetric approach is used. Left and right cells of a pair also show correlations of 0.9–0.98. Overall, surface area estimates are more highly correlated than cell perimeter because of the higher sensitivity of cell perimeter to errors in segmentation of narrow cells.
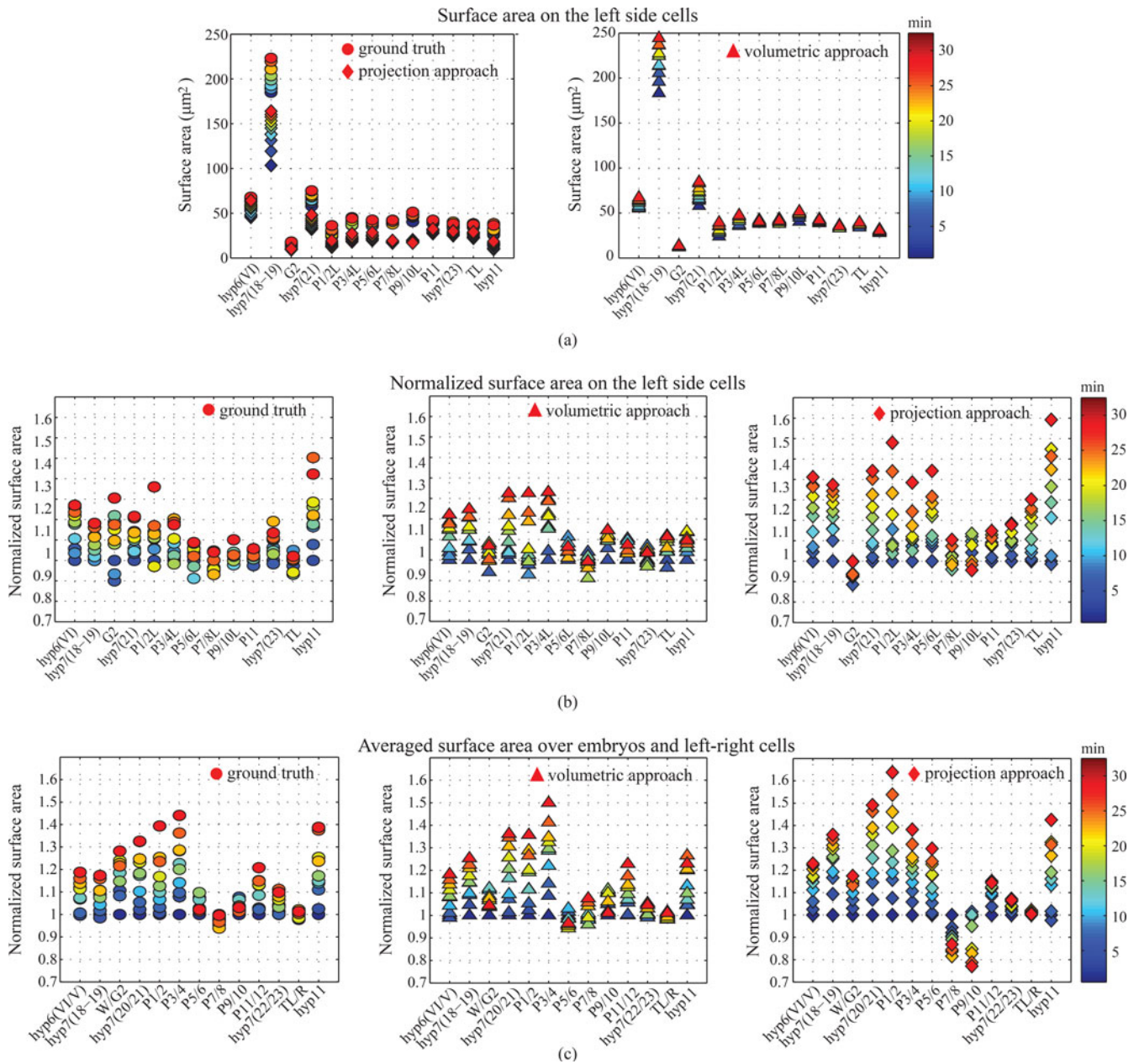
Fig. 13. Changes in epidermal cell surface area during enclosure. (a) Surface area on the left side with both approaches (Circles: ground truth, Diamonds: projection approach, Triangles: volumetric approach). (b) Normalized surface area. (c) Averaged surface area over three embryos and left-right cells.

Fig. 13(c) shows the average of normalized surface areas over three embryos and left–right cells. Both approaches show high increase in surface area for hyp6 cells, hyp7 cells 18–21, P cells 1–4, and hyp11. P cells show about 20%–30% differences in surface area and those cells are spread over more z slices. The projection approach produces accurate area measurements except when cells have a high z value. Cell surface areas in the same embryo display a correlation coefficient of 0.95–0.99 between both approaches and the ground truth.

Comparing our analyses of junctional length and area [see Figs. 10(c) and 13(c)], we can see that leading cells (anterior hyp6 and hyp7 cells) do not change in junctional length over the time of enclosure while their surface areas increase by ∼20%. The increase in surface area of hyp6 and hyp7 leading cells
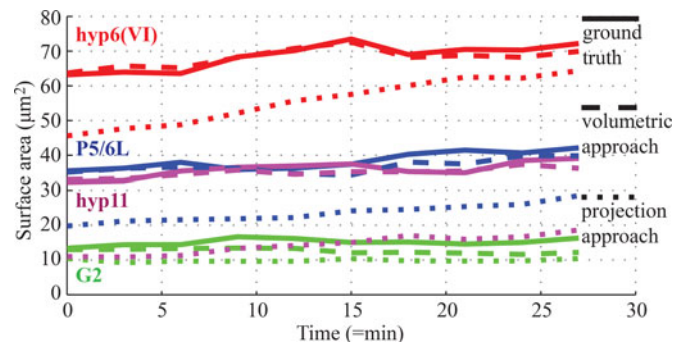

Fig. 14. Surface areas of four individual cells averaged over three embryos.
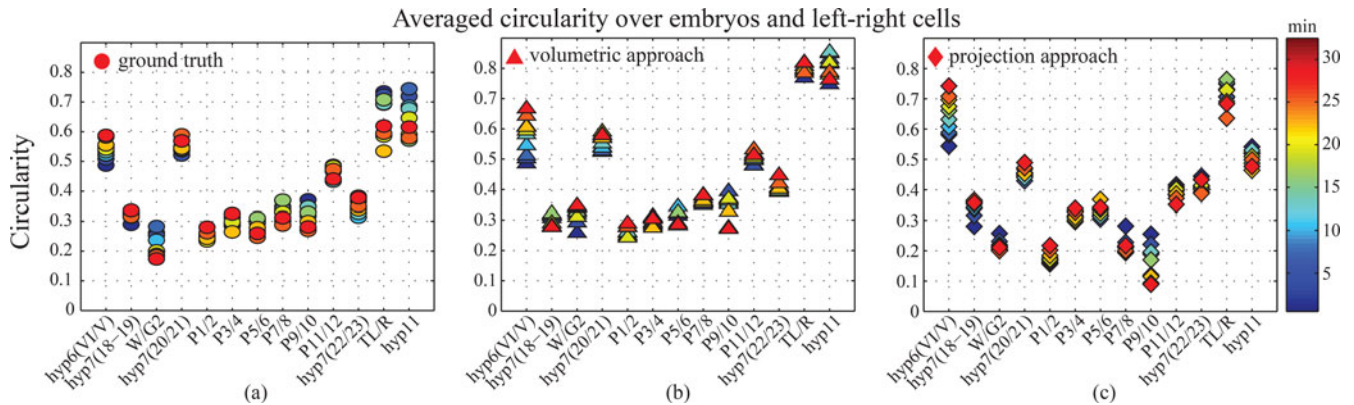
Fig. 15. Compactness of contours. Circularity factor or compactness (range: 0–1, where 1 = a circle) averaged over three embryos and left–right cells. Circularity on (a) ground truth, (b) the volumetric approach, and (c) the projection approach.

TABLE II
TOTAL SURFACE AREA OF 24 CELLS ON THE EMBRYO IN FIG. 9

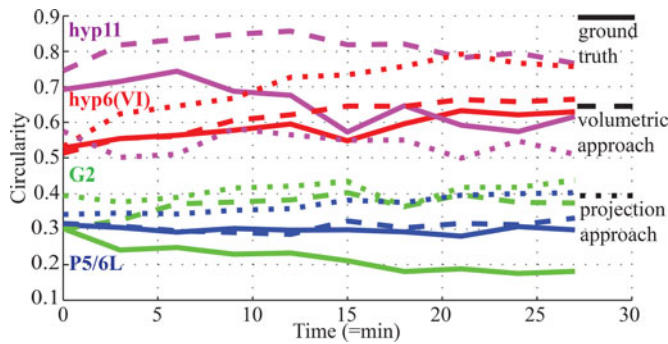| Method	Surface area (μm^2)		Increase (μm^2)
	at $t = 0$	at $t = 27$ min	
Ground truth	1065.4	1269.4	204 (19.1%)
Volumetric approach	1065.4	1295.6	230.2 (21.6%)
Projection approach	642.6	762.1	119.5 (18.6%)

Fig. 16. Circularity factor of four individual cells averaged over three embryos.

therefore reflects a change in shape from elongated to round. Similarly, ventral pocket cells hyp7(20–21) and P1–P4 increase in apical surface area by 30%–40% yet display only a 10% increase in junctional length; this disproportionate increase in area reflects a change in shape as well as an increase in cell perimeter. To quantitatively analyze trends in cell shape, we calculated a measure of compactness, i.e., the circularity factor [see Fig. 15]. The circularity factor is defined as

$$\text{Circularity} = \frac{4\pi \times \text{Surface area}}{\text{Cell perimeter}^2}. \qquad (7)$$

The circularity factor ranges within 0–1, where 1 is a circle. At $t = 0$, some ventral epidermal cells such as hyp6, hyp7(20–21), T, and hyp11 have relatively large circularity factor values (>0.5), whereas the rest are highly elongated [see Figs. 15(a) and (b)]. The projection approach shows slightly lower circularities on hyp7(20–21) and hyp11 [see Fig. 15(c)]. When we plotted the trends in circularity for four cells, we found that the three approaches show similar trends except for G2 [see Fig. 16]. The volumetric and projection approaches do not show a decrease

in circularity for G2 due to segmentation error [see Fig. 11]. During enclosure, hyp6, hyp7(20–21) increase in circularity, as do P1-4, while the ratio for other cells decreases. This reflects the large changes in shape of the anterior epidermis as it spreads anteriorly to enclose the head; in contrast, the major movement of the ventral pocket is a migration of the medial edges towards the midline, making the cells more elongated.

C. Estimation of Cell Movements from Contour Centers

As an alternative means to visualize epidermal cell movements, we tracked the centers of the cell contours [see Fig. 17]. We averaged displacements over embryos to obtain overall movement in each axis and in three dimensions. All cells show anterior movement (x axis); the anterior movement of hyp6 and hyp7 during enclosure of the head is clearly seen [see Fig. 17(b)]. Cell centers in the mid-body (P3–P8) undergo minimal x displacements (less than 1 μm), whereas cells between the mid-body and posterior show significant anterior movement. Cell displacement in the y axis [see Fig. 17(c)] clearly reveals the midline convergence of the ventral pocket during enclosure. Displacement in the z axis is largely a result of the embryonic rotation from left to right [see Fig. 17(d)]. When displacement in three dimensions is summed, the leading cells stand out as undergoing the most change in position, even though at this point they have completed their ventralward migrations. This underscores previous observations that leading cells undergo a second major phase of anterior migration during enclosure of the head [3], [31].

VI. CONCLUSIONS

Our goal is to rapidly and accurately track cell junctions in 4-D movies to allow quantitative analyses of cell shape change and movements. We have presented novel algorithms for tracking of epidermal cell junctions in *C. elegans* embryos. We use manual initialization followed by fully automatic membrane tracking to achieve accurate and efficient segmentation of epidermal membranes over time. The segmentation performance evaluated by the MAD between ground truth and segmented contours assesses the accuracy of our algorithms. The errors introduced by automatic analysis generally only compromise our
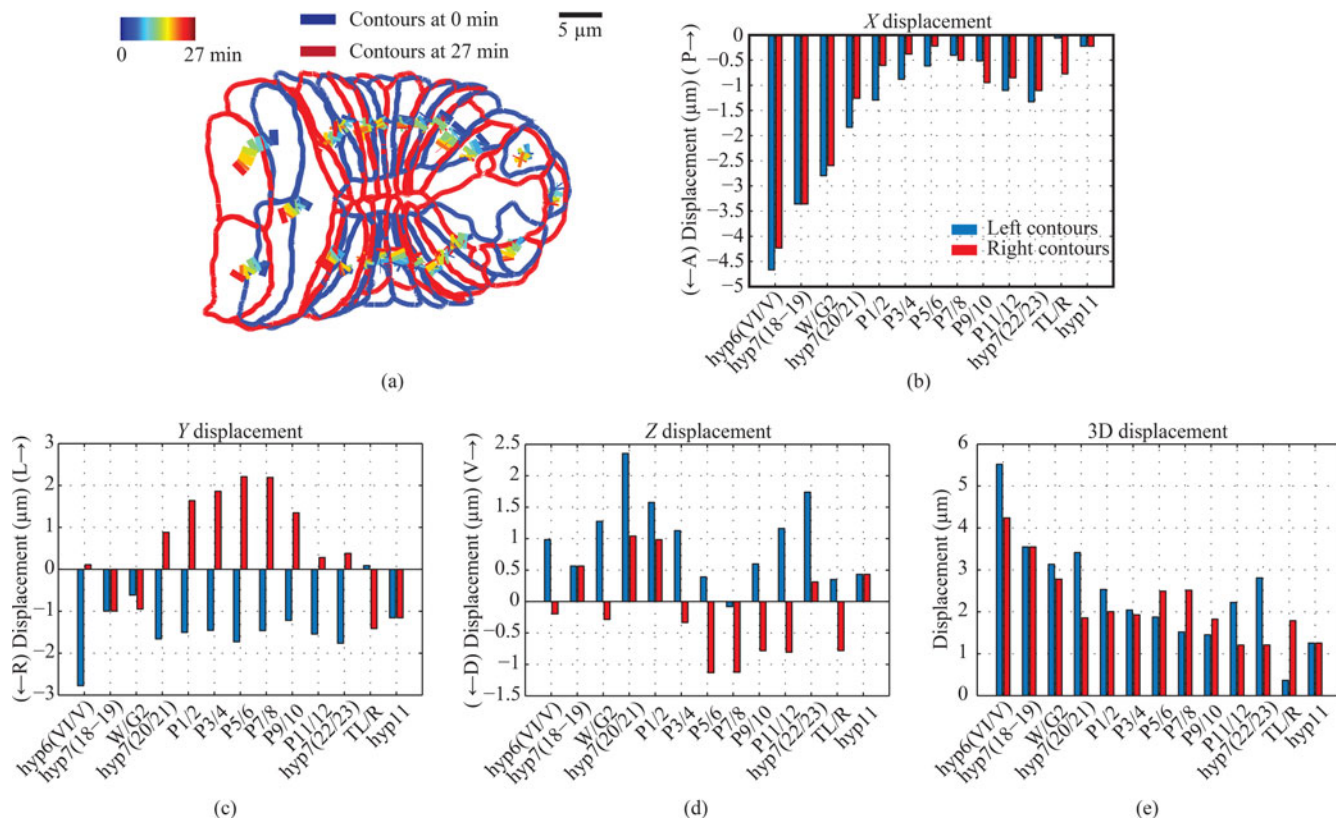
Fig. 17. Cell movement from contour centers. (a) Trajectories of contour centers (blue contour at the beginning, red contour at the end). (b) *x* displacement. Displacements of contour centers from 0 to 27 min are averaged over two datasets (blue bar: cells on the left side, red bar: cells on the right side). (c) *y* displacement. (d) *z* displacement. (e) 3-D displacement.

goal for a small number of cells that are either extremely thin in terms of apical surface, or extend across many z planes. As this is a small number of cells known to be problematic, they can be prioritized for manual curation; the vast majority of cells are well tracked.

Our quantitative analysis has been restricted to epidermal cells on one side of the embryo. Our current datasets have insufficient image SNR in the *z* slices farthest from the objective (dorsal surface in these video sequences), and lower resolution along the *z* direction. The low image SNR prevents us from analyzing cells on the bottom of the image stack. Epidermal junctions of lateral cells are also less clear due to the reduced *z* resolution. Although membrane segmentation is feasible on some lateral cells with high pixel intensities, our volumetric algorithms are not able to segment most lateral cells. Emerging microscopy methods such as Bessel sheet imaging, iSPIM or SIM [32]–[34] may allow collection of 4-D videos with the improved SNR and *z*-resolution necessary for segmentation of epidermal junctions throughout the epidermis.

Our algorithms have not dealt with fusion or division of cells. The number of epidermal cells during the period of ventral enclosure imaged here does not change. In later epidermal development, a large number of additional fusions occur that would require manual curation or new algorithms. A further challenge would be to track division of epidermal cells.

Our algorithms enable quantitative analysis of epidermal morphology and movement in *C. elegans*. The projection approach requires less initialization and computation than the volumetric approach. The projection approach shows similar length and surface area measurements to the volumetric approach except for cells that are widely spread over *z* slices. The volumetric approach with depth information produces better descriptions of cell junctions, although the volumetric approach needs more time-consuming initialization. Both methods generate robust segmentation results with less user effort than manual tracking. In conclusion, our tracking algorithms have produced the first quantitative descriptions of cellular shape during *C. elegans* epidermal enclosure. In combination with tracking of cell nuclei, these tools should assist in developing quantitative descriptions of embryonic morphogenetic processes as an essential step towards modeling of forces and cellular mechanisms.

REFERENCES

[1] Z. Bao, J. I. Murray, T. Boyle, S. L. Ooi, M. J. Sandel, and R. H. Waterston, "Automated cell lineage tracking in *Caenorhabditis elegans*," *Proc. Nat. Acad. Sci. U.S.A.*, vol. 103, no. 8, pp. 2707–2712, 2006.
[2] S. Kang, C. A. Giurumescu, A. D. Chisholm, and P. Cosman, "Automated nuclei tracking in *C. elegans* based on spherical model fitting with multiple

target tracking," in *Proc. IEEE Southwest Symp. Image Anal. Interpretation*, 2012, pp. 17–20.

[3] C. A. Giurumescu, S. Kang, T. A. Planchon, E. Betzig, J. Bloomekatz, D. Yelon, P. Cosman, and A. D. Chisholm, "Quantitative semi-automated analysis of morphogenesis with single-cell resolution in complex embryos," *Development*, vol. 139, no. 22, pp. 4271–4279, 2012.

[4] A. I. Dow, S. A. Shafer, J. M. Kirkwood, R. A. Mascari, and A. S. Waggoner, "Automatic multiparameter fluorescence imaging for determining lymphocyte phenotype and activation status in melanoma tissue sections," *Cytometry*, vol. 25, no. 1, pp. 71–81, 1996.

[5] I. Dagher and K. E. Tom, "WaterBalloons: A hybrid watershed Balloon Snake segmentation," *Image Vis. Comput.*, vol. 26, no. 7, pp. 905–912, 2008.

[6] C. Wählby, J. Lindblad, M. Vondrus, E. Bengtsson, and L. Björkesten, "Algorithms for cytoplasm segmentation of fluorescence labeled cells," *Anal. Cell. Pathol.*, vol. 24, no. 2, pp. 101–111, 2002.

[7] C. Ortiz de Solorzano, R. Malladi, S. A. Lelièvre, and S. J. Lockett, "Segmentation of nuclei and cells using membrane related protein markers," *J. Microsc.*, vol. 201, no. 3, pp. 404–415, 2001.

[8] A. Sarti, R. Malladi, and J. A. Sethian, "Subjective surfaces: A method for completing missing boundaries," *Proc. Nat. Acad. Sci.*, vol. 97, no. 12, pp. 6258–6263, 2000.

[9] A. Dufour, V. Shinin, S. Tajbakhsh, N. Guillén-Aghion, J-C. Olivo-Marin, and C. Zimmer, "Segmenting and tracking fluorescent cells in dynamic 3-D microscopy with coupled active surfaces," *IEEE Trans. Image Process.*, vol. 14, no. 9, pp. 1396–1410, Sep. 2005.

[10] K. R. Mosaliganti, R. R. Noche, F. Xiong, I. A. Swinburne, and S. G. Megason, "ACME: automated cell morphology extractor for comprehensive reconstruction of cell membranes," *PLoS Comput. Biol.*, vol. 8, no. 12: e1002780, 2012.

[11] M. T. Veeman and W. C. Smith, "Whole-organ cell shape analysis reveals the developmental basis of ascidian notochord taper," *Dev. Biol.*, vol. 373, no. 2, pp. 281–289, 2013.

[12] C. Zanella, M. Campana, B. Rizzi, C. Melani, G. Sanguinetti, P. Bourgine, K. Mikula, N. Peyriéras, and A. Sarti, "Cells segmentation from 3-D confocal images of early zebrafish embryogenesis," *IEEE Trans. Image Process.*, vol. 19, no. 3, pp. 770–781, Mar. 2010.

[13] M. A. Gelbart, B. He, A. C. Martin, S. Y. Thiberge, E. F. Wieschaus, and M. Kaschube, "Volume conservation principle involved in cell lengthening and nucleus movement during tissue morphogenesis," *Proc. Nat. Acad. Sci.*, vol. 109, no. 47, pp. 19298–19303, 2012.

[14] G. B. Blanchard, A. J. Kabla, N. L. Schultz, L. C. Butler, B. Sanson, N. Gorfinkiel, L. Mahadevan, and R. J. Adams, "Tissue tectonics: Morphogenetic strain rates, cell shape change and intercalation," *Nat. Methods*, vol. 6, no. 6, pp. 458–464, 2009.

[15] A. C. Martin, M. Kaschube, and E. F. Wieschaus, "Pulsed contractions of an actinmyosin network drive apical constriction," *Nature*, vol. 457, no. 7228, pp. 495–499, 2008.

[16] B. Aigouy, R. Farhadifar, D. B. Staple, A. Sagner, J. C. Röper, F. Jülicher, and S. Eaton, "Cell flow reorients the axis of planar polarity in the wing epithelium of Drosophila," *Cell*, vol. 142, no. 5, pp. 773–786, 2010.

[17] R. Fernandez-Gonzalez and J. A. Zallen, "Oscillatory behaviors and hierarchical assembly of contractile structures in intercalating cells," *Phys. Biol.*, vol. 8, no. 4, 045005, 2011.

[18] F. Bosveld, I. Bonnet, B. Guirao, S. Tlili, Z. Wang, A. Petitalot, R. Marchand, P. L. Bardet, P. Marcq, F. Graner, and Y. Bellaïche, "Mechanical control of morphogenesis by Fat/Dachsous/Four-jointed planar cell polarity pathway," *Science*, vol. 336, no. 6082, pp. 724–727, 2012.

[19] M. Kass, A. Witkin, and D. Terzopoulos, "Snakes: Active contour models," *Int. J. Comput. Vis.*, vol. 1, no. 4, pp. 321–331, 1988.

[20] C. Liu, J. Yuen, A. Torralba, J. Sivic, and W. T. Freeman, "SIFT flow: Dense correspondence across different scenes," in *Proc. Eur. Conf. Comput. Vis.*, 2008, pp. 28–42.

[21] C. Lee, S. Kang, A. D. Chisholm, and P. C. Cosman, "Automated cell junction tracking with modified active contours guided by SIFT flow," in *IEEE Int. Symp. Biomed. Imag.*, 2014, pp. 290–293.

[22] N. Gorfinkiel, G. B. Blanchard, R. J. Adams, and A. M. Arias, "Mechanical control of global cell behaviour during dorsal closure in Drosophila," *Development*, vol. 136, no. 11, pp. 1889–1898, 2009.

[23] J. Solon, A. Kaya Copur, J. Colombelli, and D. Brunner, "Pulsed forces timed by a ratchet-like mechanism drive directed tissue movement during dorsal closure," *Cell*, vol. 137, no. 7, pp. 1331–1342, 2009.

[24] R. Totong, A. Achilleos, and J. Nance, "PAR-6 is required for junction formation but not apicobasal polarization in *C. elegans* embryonic epithelial cells," *Development*, vol. 134, no. 7, pp. 1259–1268, 2007.

[25] B. D. Lucas and T. Kanade, "An iterative image registration technique with an application to stereo vision," in *Proc. Int. Joint. Conf. Artif. Intell.*, 1981, vol. 81, pp. 674–679.

[26] D. G. Lowe, "Distinctive image features from scale-invariant keypoints," *Int. J. Comput. Vis.*, vol. 60, no. 2, pp. 91–110, 2004.

[27] W. Geng, P. Cosman, C. C. Berry, Z. Feng, and W. R. Schafer, "Automatic tracking, feature extraction and classification of *C. elegans* phenotypes," *IEEE Trans. Biomed. Eng.*, vol. 51, no. 10, pp. 1811–1820, Oct. 2004.

[28] D. J. Williams and M. Shah, "A fast algorithm for active contours and curvature estimation," *CVGIP: Image Understanding*, vol. 55, no. 1, pp. 14–26, 1992.

[29] J. D'Errico. (2006). Understanding Gridfit. [Online]. Available: http://www.mathworks.com/matlabcentral/fileexchange/8998

[30] V. Chalana, D. T. Linker, D. R. Haynor, and Y. Kim, "A multiple active contour model for cardiac boundary detection on echocardiographic sequences," *IEEE Trans. Med. Imag.*, vol. 15, no. 3, pp. 290–298, Jun. 1996.

[31] E. M. Williams-Masson, A. N. Malik, and J. Hardin, "An actin-mediated two-step mechanism is required for ventral enclosure of the *C. elegans* hypodermis," *Development*, vol. 124, no. 15, pp. 2889–2901, 1997.

[32] T. A. Planchon, L. Gao, D. E. Milkie, M. W. Davidson, J. A. Galbraith, C. G. Galbraith, and E. Betzig, "Rapid three-dimensional isotropic imaging of living cells using Bessel beam plane illumination," *Nat. Methods*, vol. 8, no. 5, pp. 417–423, 2011.

[33] Y. Wu, A. Ghitani, R. Christensen, A. Santella, Z. Du, G. Rondeau, Z. Bao, D. Colón Ramos, and H. Shroff, "Inverted selective plane illumination microscopy (iSPIM) enables coupled cell identity lineaging and neurodevelopmental imaging in *Caenorhabditis elegans*," *Proc. Nat. Acad. Sci.*, vol. 108, no. 43, pp. 17708–17713, 2011.

[34] L. Gao, L. Shao, C. D. Higgins, J. S. Poulton, M. Peifer, M. W. Davidson, X. Wu, B. Goldstein, and E. Betzig, "Noninvasive imaging beyond the diffraction limit of 3D dynamics in thickly fluorescent specimens," *Cell*, vol. 151, no. 6, pp. 1370–1385, 2012.